European Journal of Mechanics / A Solids 95 (2022) 104652

Contents lists available at ScienceDirect

European Journal of Mechanics / A Solids

journal homepage: www.elsevier.com/locate/ejmsol

Analytical shakedown, ratchetting and creep solutions for idealized twin-wall blade components subjected to cyclic thermal and centrifugal loading

Christos Skamniotis *, Alan C.F. Cocks

Department of Engineering Science, University of Oxford, Parks Road, Oxford, OX7 6DP, UK

ARTICLE INFO

Keywords:
Shakedown
Ratchetting
Out-of-phase thermomechanical loading
Creep
Cyclic plasticity
Temperature dependent yield strength
Double wall transpiration cooled turbine blades
Thermoelastic analysis
Nickel alloys

ABSTRACT

Double-wall transpiration cooling systems offer the potential for performance improvements over conventional single wall systems in aerospace applications. Here we idealise the geometry in terms of a constrained 2 bar system which allows the development of analytical expressions for the entire range of possible mechanical responses under out-of-phase thermomechanical loading. The application of Koiter's shakedown theorem along with equilibrium is a powerful strategy for identifying mechanisms by which the structure can incrementally collapse (ratchetting). We show that twin wall systems with zero mechanical loading can ratchet in the compressive direction when severe thermal mismatch occurs, and that ratchetting is replaced by reverse plasticity as the bar thickness difference increases. Mechanisms exist where plastic strains do not occur at the extremes of the loading cycle. The degradation of yield strength of Ni alloys with temperature modifies drastically the response, while additional creep induced ratchetting and creep failure processes are shown to occur at extreme temperatures within a cycle. Our solutions aim to provide physical insight into the response of double-wall transpiration cooled Ni-based turbine blades.

1. Introduction

Double-wall transpiration cooling systems (DWTCs) aim to allow gas turbines to operate at temperatures beyond current levels, promising further increases in fuel efficiency and specific power output (Sunden and Xie, 2010). The implementation of DWTCs in gas turbine blades is of high engineering significance, as engine efficiency generally depends on the level of thermomechanical loading that these components can withstand (Reed, 2008). DWTCs contain an inner cool wall and an outer hot wall that accommodate impingement holes and film holes, respectively, through which coolant circulates to pick-up heat from the metal and provides thermal protection from the external heat flux driven by the flow of the surrounding hot gas (Murray et al., 2019); an example of a DWTC turbine blade is given in Fig. 1a. Despite the outstanding aerothermal characteristics of DWTCs (Murray et al., 2018), there remain structural integrity implications which need to be investigated.

Thermomechanical fatigue (TMF) driven by the combination of through thickness thermal gradients (thermal bending stresses) and centrifugal loading (mechanical tensile stresses) has been a longstanding concern in conventional single wall blades (Kauss et al., 2019; Sadowski and Golewski, 2012). Recent studies indicate that such concerns increase for DWTC blades, as additional membrane thermal stresses are generated due to the kinematic coupling of the two walls (through the pedestals) (Skamniotis and Cocks, 2020; Skamniotis and Cocks, 2021a) as well as the inherent thermal mismatch between the walls (Skamniotis et al., 2021). A typical temperature field and the corresponding elastic stress field for superimposed centrifugal loading (taken from papers by the authors (Skamniotis and Cocks, 2021c; Skamniotis et al., 2021)) are shown in Fig. 1b–c for a repeating unit cell of a DWTC blade. The implications of thermal loading on fatigue at stress raisers i.e. film/impingement holes, has been recently studied in (Skamniotis and Cocks, 2021b) through a series of local Neuber type solutions and verified full finite element (FE) cycle-by-cycle inelastic solutions.

Global failure mechanisms, on the other hand, such as incremental structural collapse (ratchetting) have not been explored; to the author's knowledge, this also applies to conventional single wall blades. Indeed, calculations of this type have mainly targeted nuclear applications, e.g. pressure vessels, heat exchangers and reactors (Adibi-Asl and Reinhardt, 2011b; Ma et al., 2021), where significant cyclic thermomechanical stresses can be generated during operation, with the range of behaviour illustrated through the construction of interaction (often referred to as

* Corresponding author.
E-mail address: christos.skamniotis@eng.ox.ac.uk (C. Skamniotis).

https://doi.org/10.1016/j.euromechsol.2022.104652
Received 26 October 2021; Received in revised form 3 May 2022; Accepted 11 May 2022
Available online 17 May 2022

Nomenclature

Abbreviations

DWTC	double wall transpiration cooling
FE	Finite elements
2D	two-dimensional
3D	three-dimensional
SCF	stress concentration factor

Symbols, Thermal

T_h	hot bar temperature (°C)
T_c	cool bar temperature (°C)
T_0	room temperature (°C)
T_o	reference temperature for creep law (°C)
ΔT	thermal difference between bars (°C)

Structural

t_h	hot bar thickness (mm)
t_c	cool bar thickness (mm)
$\bar{t}_h$	hot bar thickness normalised by total structural thickness
$\bar{t}_c$	cool bar thickness normalised by total structural thickness

Material

E	Elastic Modulus (MPa)
ν	Poisson's ratio
a	thermal expansion coefficient (m/m•K)
a_h	hot bar thermal expansion coefficient (m/m•K)
a_c	cool bar thermal expansion coefficient (m/m•K)
Q	activation energy (KJ/mol)
R	universal gas constant (J/mol• K)
$\dot{\varepsilon}_o$	reference creep rate (1/h)
σ_o	reference stress for creep law (MPa)
n	creep power law exponent
σ_y	(constant) yield stress (MPa)
σ_{y_T}	temperature dependent yield stress (MPa)
σ_{y_h}	hot bar yield stress (MPa)
σ_{y_c}	cool bar yield stress (MPa)
σ_{y_0}	room temperature yield stress (MPa)
$\bar{\sigma}_y$	average yield stress (MPa)

Mechanical

$p(\tau)$	instantaneous mechanical stress/pressure at an instance, τ, through the cycle (MPa)
$\sigma_T(\tau)$	instantaneous thermoelastic stress at an instance, τ, through the cycle (MPa)
p	maximum mechanical stress/pressure occurring at steady state regime of the cycle (MPa)
σ_T	maximum thermoelastic stress occurring at steady state regime of the cycle (MPa)
p^s	maximum mechanical stress/pressure at a shakedown (SR or PR) boundary (MPa)
σ_T^s	maximum thermoelastic stress at a shakedown (SR or PR) boundary (MPa)
$\widehat{\sigma}_h(\tau)$	instantaneous elastic stress in hot bar (MPa)
$\widehat{\sigma}_c(\tau)$	instantaneous elastic stress in cool bar (MPa)
$\widehat{\sigma}_h$	extreme/maximum compressive elastic stress in hot bar (MPa)
$\widehat{\sigma}_c$	extreme/maximum elastic stress in cool bar (MPa)
$\sigma_h(\tau)$	instantaneous stress in hot bar (MPa)
$\sigma_c(\tau)$	instantaneous stress in cool bar (MPa)
p_{CR}	maximum mechanical stress/pressure at creep-ratchetting failure (CR) line (MPa)
p_C	maximum mechanical stress/pressure at global creep failure (C) line (MPa)
$\dot{\varepsilon}_{cr}$	creep strain rate (1/h)

Time

t_{cycle}	cyclic time period (h)
$t_{p-trans}$	transient time period for mechanical loading/unloading (h)
$t_{\Delta T-trans}$	transient time period for thermal loading/unloading (h)
t_{dwell}	steady state temperature/creep dwell time period (h)
τ_i	time instance identifier
d	thermal delay factor for out-of-phase loading

Failure

$N_{0.1}$	cycles required for 0.1 total creep strain accumulation
$\varepsilon_{cr_{0.1}}$	failure strain

Bree type or Brussel) diagrams (Bree, 1967; A. R. Ponter, Karadeniz and Carter, 1990). An assessment of DWTC systems is essential, not only because coupling of the walls can trigger ratchetting mechanisms (Segle et al., 2016), but also because design will benefit from an understanding of where the in-service loading conditions lie with respect to the ratchet boundaries. Here we will attempt to address this knowledge gap, by firstly constructing analytical solutions for the boundaries between shakedown, ratchetting and reversed plasticity for a 2D 2-bar structure (Fig. 1d) under thermomechanical (TM) loading conditions that are relevant to DWTC blades.

The 2-bar structure, along with the Bree plate and plate-hole idealisations have been used by various authors to understand-explain ratchetting (Bree, 1967; Hübel, 1996; Segle et al., 2016), to develop extended shakedown theory (A. Ponter and Cocks, 1984; A. Ponter and Karadeniz, 1985a, 1985b), to identify the role of material and load sequencing effects (Bradford, 2012, 2017; Ng and Moreton, 1987), as well as to advance-validate direct/numerical tools for the ratchet boundary determination (Adibi-Asl and Reinhardt, 2010, 2011a, 2011b; Ma et al., 2021; K. Spiliopoulos and Panagiotou, 2014). Most of these studies, however, focus on either cyclic thermal loading combined with constant mechanical loading or completely in-phase/completely out-of-phase TM loading, which do not relate to the type of loading experienced by transpiration systems. Also, material models in these studies and the way in which the properties change with temperature are not representative of the behaviour of Ni based superalloys used in turbine components. Here we focus on the effect of the ratio of the thickness of the 2 bars (reflecting role of wall thickness ratio in a transpiration system – which is a key design variable) and explore the range of loading cycles (phase angles and cycle times) and material constitutive behaviour relevant to the design of transpiration cooling systems.

All the above aspects will be studied here for a wide range of thickness ratios in the 2-bar system, providing physical insights that may be difficult to gain through current numerical methods. We will demonstrate that by feeding the elastic stress solution into Koiter's kinematic upper bound theorem (Koiter, 1960) and selecting mechanisms that give rise to stress states that satisfy equilibrium, full interaction diagrams can be constructed in a straightforward manner. We firstly describe the rational for the idealisations used, along with the analysis methods (Section 2). Thereafter we identify ratchet mechanisms based on a constant yield stress and then indicate how these mechanisms change when the yield stress follows a temperature dependent behaviour typical to Ni alloys, followed by analysis of creep effects during the high temperature part of a cycle (Section 3). A general discussion of the analysis and results is finally provided in Section 4, followed by conclusions.

2. Problem idealisation and methods

2.1. Thermomechanical loading

The simplified 2-bar problem (Fig. 1d) captures many of the features of the more complex problem shown in Fig. 1b, in that thermal loading is manifested by the thermal difference, $\Delta T = T_h - T_c$, between the hot and cool walls/bars while the two walls/bars are kinematically constrained to extend by the same amount. Also mechanical loading p is used here to model the centrifugal/body forces applied by the remainder of the turbine blade, which scale with material density, ρ, rotational speed squared, ω^2, and a length parameter, L (see Fig. 1b); details of how these quantities should be computed to determine p are available in Skamniotis et al. (2021); such calculations are not performed here since the entire possible range of p will be considered.

Features not captured by our 2-bar idealisation are: (a) the effect of holes, (b) the biaxiality of nominal thermal stresses in the actual 3D plates (mechanical loading is uniaxial), and (c) the thermal gradient through the hot wall thickness (see Fig. 1b). A discussion of the potential effects of these features on ratchetting, along with justification of the 2-bar idealisation will be provided in Section 4.

The type of simplified TM loading cycles considered here, which capture the major features of those experienced by turbine blades, are shown in Fig. 2a–b in load-time and load-load space. The instantaneous values of thermal and mechanical loading are here referred to as $\Delta T(\tau)$ and $p(\tau)$, whereas the maximum values that apply during the steady state regime of the cycle are referred to as ΔT and p. Both thermal and mechanical loading involve a linear increase, followed by a steady state and then a linear decrease (see Fig. 2a). The key feature here is that the time for the transition of the thermal cycle to and from the steady state can be different to the $p(\tau)$ transitions, e.g. the maximum value p can occur before the maximum value ΔT, which implies the possible existence of four load vertices/extremes in load-load space (4, 1, 2 and 3 in Fig. 2b) and five vertices in load-time space (4, 1, 2, 2′ and 3 Fig. 2a); note that the decrease of $\Delta T(\tau)$ and $p(\tau)$ is assumed to begin at the same instance 2′ and that in-phase loading involves two vertices in load-load space and three vertices in load-time space (see Fig. 2b). By using a total cyclic time period, t_{cycle} (up to instance 4), and a $p(\tau)$ transient time, $t_{p(\tau)-trans}$ (from 4 to 1 or from 2′ to 3), the above out-of-phase characteristic is replicated by using a $\Delta T(\tau)$ transient time, $t_{\Delta T(\tau)-trans} = d \bullet t_{p(\tau)-trans}$, where $d \geq 1$ is a thermal delay factor. Note that in-phase loading implies $d = 1$ and two load vertices/extremes in load-load space (2 and 4 in Fig. 2b) and three in load-time space (2, 2’ and 4 in Fig. 2a).

The factor d is introduced here as a more realistic idealisation of out-of-phase loading experienced by turbine blades, compared to previous out-of-phase idealisations (Bradford, 2017) where the entire thermal cycle was translated in time with respect to the load cycle, and reflects the fact that in practice the peak turbine speed in an engine occurs before the blade reaches its peak temperature and during landing the engine speed drops faster than the temperature. Data on the out-of-phase angle that occurs in turbine blades in-service are sparse. Kauss et al. reported (Kauss et al., 2019) that it can take 600 s–1000 s for the temperatures to settle in a conventional turbine blade during start-up, whereas the increase of ω is typically an order of magnitude faster. This is consistent with our idealisation and suggests that a range of d values should be considered.

2.2. Elastic solution

The instantaneous elastic stresses, $\widehat{\sigma}_h(\tau)$, $\widehat{\sigma}_c(\tau)$ in the hot and cool bars (Fig. 1d), as a function of the instantaneous thermal and mechanical loading are determined by the kinematic condition for equal total strain (Eq (1)) and equilibrium (Eq (2)):

$$\frac{\widehat{\sigma}_h(\tau)}{E_h} + \frac{a_h T_h(\tau)}{d} = \frac{\widehat{\sigma}_c(\tau)}{E_c} + \frac{a_c T_c(\tau)}{d} \tag{1}$$

$$\widehat{\sigma}_h(\tau)\bar{t}_h + \widehat{\sigma}_c(\tau)\bar{t}_c = p(\tau) \tag{2}$$

where E_h, E_c and a_h, a_c are the temperature dependent Young’s moduli and thermal expansion coefficients of the 2 bars, whereas $\bar{t}_c = t_c/(t_c + t_h)$ and $\bar{t}_h + \bar{t}_c = 1$. Solving Eqs (1) and (2) for $\widehat{\sigma}_h(\tau)$ gives

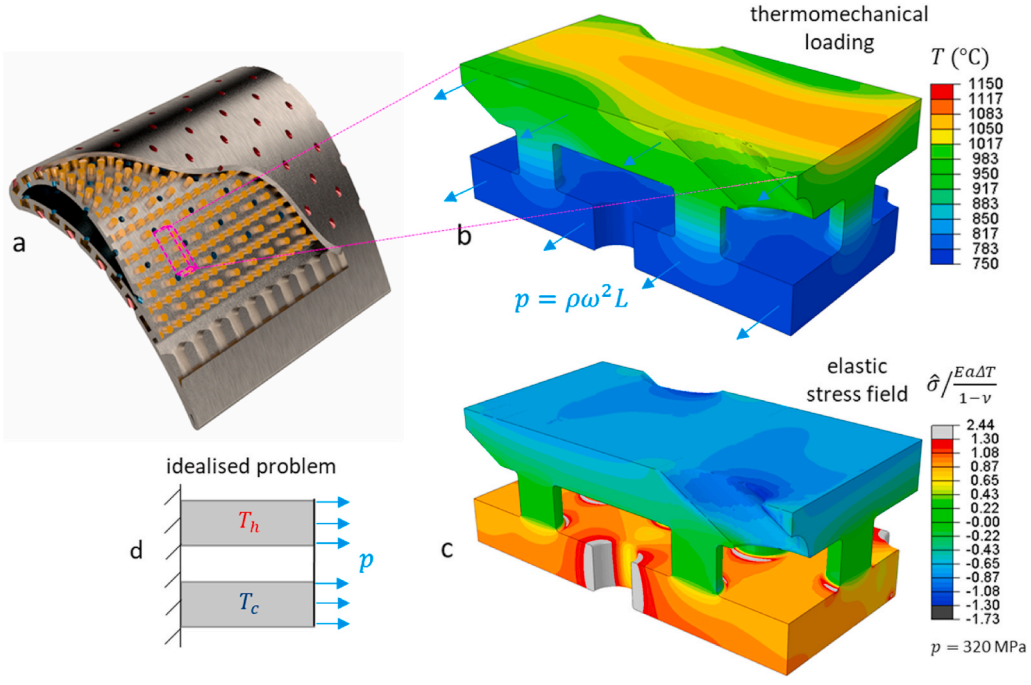

Fig. 1. (a) DWTC turbine blade model taken from (Murray et al., 2017). (b) Steady state temperature field in a simplified repeating unit block of Fig. 1a, with centrifugal loading, p, indicated; taken from (Skamniotis et al., 2021). (c) Elastic stress field corresponding to the loading case of Fig. 1b; reproduced from (Skamniotis and Cocks, 2021c). (d) Two-bar idealisation of thermomechanical loading used in the present study.

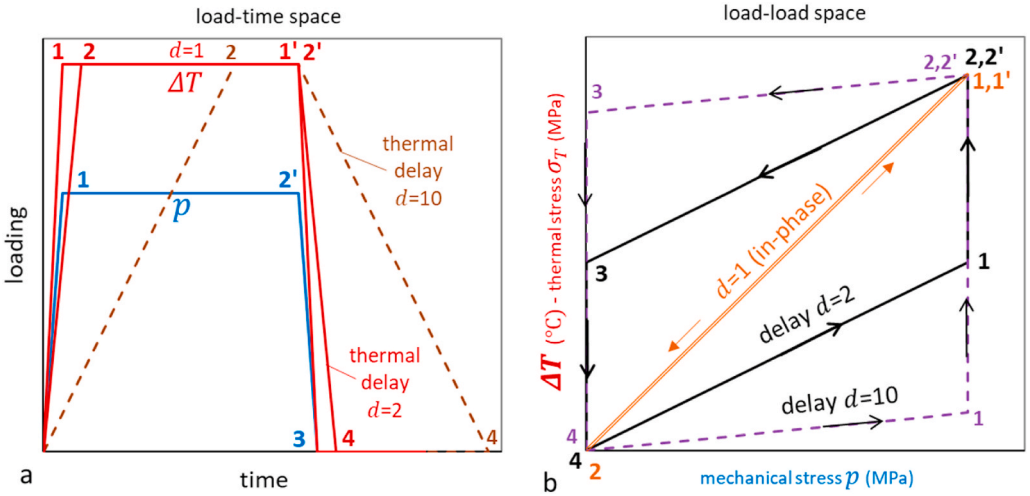

Fig. 2. (a) Examples of the idealised thermomechanical loading cycle for $d = 1$, $d = 2$ and $d = 10$ in load-time space; numbers indicate the vertices/extremes of the cycle. (b) Corresponding cycles in load-load space, for the cases $d = 1$, $d = 2$, $d = 10$. The maximum mechanical stress p is induced by the engine rotation speed, ω; the maximum thermal stress, σ_T, through the cycle is induced by the bar (maximum) thermal difference, ΔT.

$$\widehat{\sigma}_h(\tau) = \frac{1}{d}\frac{a_c T_c(\tau) - a_h T_h(\tau)}{\frac{1}{E_h} + \frac{t_h}{t_c E_c}} + p(\tau) \quad (T \text{ dependent } E,\ \alpha) \tag{3}$$

$$\widehat{\sigma}_h(\tau) = -\frac{\bar{t}_c E \alpha \Delta T}{d} + p \quad (\text{constant } E,\ \alpha) \tag{4}$$

where Eq (4) applies in the idealised case of $E_h = E_c = E$ and $a_h = a_c = \alpha$. For the Ni alloys of interest here $E_h < E_c$ and $a_h > a_c$, since the Young's modulus, E, reduces by ~40% from room temperature to 1100 °C, whereas the thermal expansion coefficient, α, almost doubles (Dye et al., 2004). This implies that the increase of $|a_c T_c - a_h T_h|$ in Eq (3) due to $a_h > a_c$ (note $a_c T_c - a_h T_h < 0$) dominates over the increase of $\frac{1}{E_h} + \frac{t_h}{t_c E_c}$ associated with the reduction of E_h and E_c with temperature. As a result, the actual thermal stress magnitude computed by Eq (3) is typically around 1.37 times higher than the corresponding value $|-\bar{t}_c E \alpha \Delta T|$ when constant values of E, α for a reference temperature are used in Eq (4) (Skamniotis and Cocks, 2021c), in the range $\Delta T < 600$ °C. To compensate for this effect, here we will use a reference value $\alpha = 1.74 \bullet 10^{-5}$ (1/°C) for CMSX-4 at 700 °C and scale it by 1.37 in Eq (4). To simultaneously account for the increase of thermal stresses by the factor $1/(1-\nu)$ in the actual 3D situation with respect to the present 2D idealisation, we will also use a reference value of $E = 100$ GPa for CMSX-4 at 700 °C and scale it by $1/(1-\nu)$ in Eq (4), for a reference Poisson's ratio, $\nu = 0.4$; the same approach was used by Bree (1967). This corresponds to $E\alpha = 3.97$ MPa/°C in Eq (4).

The above corrections are applied here in order to reproduce the thermoelastic stress range in the 3D plates of an actual double-wall transpiration system with temperature dependent E and α. Using constant values of E, α in Eq (4) is preferred here over using the temperature dependent values in Eq (3), as the latter complicates the shakedown-ratchet calculations without providing any additional physical insight. Here we will use the elastic stress solutions:

$$\text{Instantaneous values}: \quad \widehat{\sigma}_h(\tau) = p(\tau) - \bar{t}_c \sigma_T(\tau)/d \quad \text{and} \quad \widehat{\sigma}_c(\tau) = p(\tau) + \bar{t}_h \sigma_T(\tau)/d \tag{5a}$$

$$\text{Maximum values (at steady state)}: \quad \widehat{\sigma}_h = p - \bar{t}_c \sigma_T \quad \text{and} \quad \widehat{\sigma}_c = p + \bar{t}_h \sigma_T \tag{5b}$$

for the hot and cool bars, with the maximum thermoelastic stress scaling with $\sigma_T = E\alpha\Delta T$. At point 4 in the cycle (Fig. 2b), when both thermal and mechanical loading are zero, the elastic solution gives zero stresses in the bars, i.e. $\widehat{\sigma}_h(\tau) = \widehat{\sigma}_c(\tau) = 0$. Under cyclic conditions the instantaneous stresses, $\widehat{\sigma}_h(\tau)$ and $\widehat{\sigma}_c(\tau)$, cycle between the extreme values, $\widehat{\sigma}_h$, $\widehat{\sigma}_c$ and zero, following a path determined by the form of the cycle shown in Fig. 2.

2.3. Plasticity and creep models

We consider the plastic and creep behaviour of the CMSX-4 Ni alloy (Nathal et al., 2015; Sengupta et al., 1994), illustrated in Fig. 3a–b. A trilinear fit is used to idealise the yield stress dependence with temperature, including a constant value, $\sigma_{y_0} = 805$ MPa, in the cold regime 0–700 °C, followed by a sharp increase of yield stress to a maximum of 960 MPa at 720 °C and then a linear negative dependence, $\sigma_{y_T} = c_1 T + c_2$, in the hot regime 720–1200 °C (see Fig. 3a). We assume perfect plasticity and the same yield stress in compression and tension. The creep power law:

$$\dot{\varepsilon}_{cr} = \dot{\varepsilon}_o \,\mathrm{sgn}(\sigma) \left(\frac{|\sigma|}{\sigma_o}\right)^n \exp(x) \tag{6}$$

is used to idealise the creep strain rate, $\dot{\varepsilon}_{cr}$, versus constant stress, σ, data at a given temperature T in Fig. 3b, where $x = -\frac{Q}{R}\left(\frac{1}{T} - \frac{1}{T_o}\right)$, the set of constants, $\dot{\varepsilon}_o = 1/\text{h}$, $\sigma_o = 800$ MPa, $T_o = 830$ °C, determines the constant creep strain rate under a constant stress and constant temperature, $n = 10$ is the creep exponent, $Q = 400$ kJ/mol is the activation energy and $R = 8.31$ (J/mol•K) is the gas constant. When plasticity and creep are both active, the total strain rate, $\dot{\varepsilon}$, of a bar is determined (for small strains) by the superposition of the thermal, elastic, plastic and creep rates:

$$\dot{\varepsilon} = \dot{\varepsilon}_T + \dot{\varepsilon}_e + \dot{\varepsilon}_p + \dot{\varepsilon}_{cr} \tag{7}$$

2.4. Shakedown-ratchet calculations

The underlying assumption of our shakedown solutions is that plastic strains accumulate at discrete instances through the cycle. In most cases ratchetting occurs at different instants in the cycle for the 2 bars. Koiter's kinematic upper bound theorem (Koiter, 1960) states that for a prescribed loading cycle the structure will ratchet or suffer reverse plastic straining if a mechanism of compatible plastic strains over the cycle can be found such that the total work done by the elastic stress variations over a cycle is greater than the total plastic energy dissipated over the cycle. In design, it proves more instructive to express this theorem in a modified form to provide a bound on the boundary between shakedown and ratchetting or shakedown and reversed plasticity – on a plot of

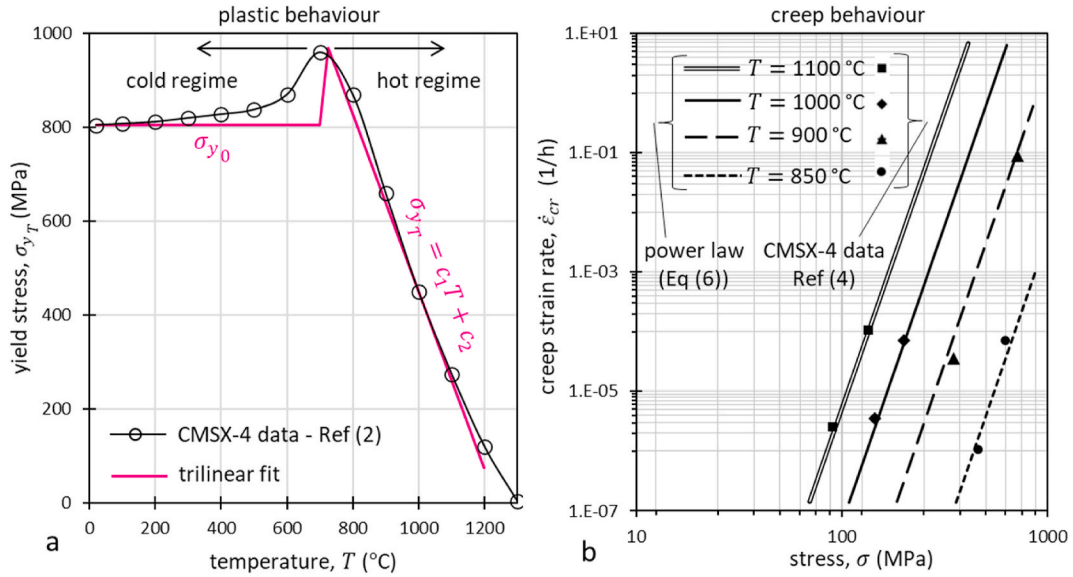

Fig. 3. (a) Yield stress dependence with temperature for CMSX-4, including test data (taken from Sengupta et al. (1994)) and trilinear fit ($c_1 = -1.88$, $c_2 = 2336$). (b) Isothermal creep rates at different stress levels for CMSX-4, including test data (taken from Nathal et al. (2015)) and power law fit. Test data correspond to the ⟨001⟩ crystallographic orientation.

maximum thermal stress, σ_T, against maximum mechanical stress, p, in the current context. In many situations it is appropriate to assume a mechanism whereby plastic deformation only occurs at two instances in the cycle. For the 2 bar structure we can express the instantaneous elastic stress solutions, $\widehat{\sigma}_h(\tau)$ and $\widehat{\sigma}_c(\tau)$ (Eq (5a)) in the 2 bars, as a function of the maximum stresses/loads, p and σ_T (Eq (5b)), in the form:

$$\widehat{\sigma}_h(\tau) = a(\tau)\, p - b(\tau)\bar{\imath}_c \sigma_T/d \tag{8a}$$

and

$$\widehat{\sigma}_c(\tau) = a(\tau)\, p + b(\tau)\bar{\imath}_h \sigma_T/d \tag{8b}$$

where τ is the instant in the cycle and $a(\tau)$ and $b(\tau)$ depend on the detailed form of the cycle (Fig. 2), and can be expressed in terms of the quantity d introduced in Section 2.1. If σ_T^s, p^s and $\widehat{\sigma}_h^s(\tau_i)$, $\widehat{\sigma}_c^s(\tau_j)$ are the values of σ_T, p and $\widehat{\sigma}_h(\tau)$, $\widehat{\sigma}_c(\tau)$ at the shakedown limit, Koiter's theorem takes the form:

$$\widehat{\sigma}_h^s(\tau_i) d\varepsilon_{p_h} t_h + \widehat{\sigma}_c^s(\tau_j) d\varepsilon_{p_c} t_c \le \sigma_{y_h}(\tau_i) d\varepsilon_{p_h} t_h + \sigma_{y_c}(\tau_j)\, d\varepsilon_{p_c} t_c \tag{9}$$

where $d\varepsilon_{p_h}$ and $d\varepsilon_{p_c}$ denote the plastic strain increments associated with the assumed mechanism at the two instances τ_i and τ_j in the cycle in the hot and cool wall, respectively, and $\sigma_{y_h}(\tau_i)$, $\sigma_{y_c}(\tau_j)$are yield stresses corresponding to these instances and locations. By taking Eq (8) into account, Eq (9) can be re-written as:

$$p^s\left[a(\tau_i)\bar{\imath}_h d\varepsilon_{p_h} - a(\tau_j)\bar{\imath}_c d\varepsilon_{p_c}\right] + \frac{\sigma_T^s \bar{\imath}_h \bar{\imath}_c}{d}\left[b(\tau_j) d\varepsilon_{p_c} - b(\tau_i) d\varepsilon_{p_h}\right] \le \sigma_{y_h}(\tau_i) d\varepsilon_{p_h} \bar{\imath}_h + \sigma_{y_c}(\tau_j) d\varepsilon_{p_c} \bar{\imath}_c \tag{10}$$

The upper bound to the shakedown boundary given by Eq (10) only depends on the form of the mechanism and not its scale. For a given form of mechanism and constant values of the yield strength in the hot and cold bars, (10) gives a straight line in $p - \sigma_T$ space, below which any point $p^s - \sigma_T^s$ on the shakedown boundary lies. The shakedown boundary is formed by the inner envelope of the lines for all possible mechanisms, and is convex. If the yield strength is a function of temperature, as in Fig. 3a, the yield stresses in (10) will correspond to the current temperatures at the instants of local plastic deformation, τ_i and τ_j, and, for a given mechanism, the line below which shakedown occurs will have a shape that reflects the temperature dependence of the yield strength. When the assumed mechanism is such that plasticity occurs on complete removal of the thermal and mechanical loads, e.g. instance 4 in Fig. 2b, both $a(\tau)$ and $b(\tau)$ in (10) are equal to zero at this instant, but the corresponding energy dissipation term remains.

The above methodology applies for classical (elastic) shakedown situations. Often in design a certain amount of reversed plastic straining can be tolerated locally within a structure, but a small ratchet strain per cycle can lead to significant deformation over a few hundred cycles, and cannot be allowed. It is then important to determine the load conditions at which there is a transition from reversed plasticity to ratcheting (where, in this scenario, the ratchet mechanism generally involves significant reversed plastic straining during a cycle). This is often referred to as the plastic shakedown limit, and we designate the resulting boundary as the (PR) boundary. The extended shakedown method developed by Ponter (A. Ponter and Karadeniz, 1985a; 1985b) can be used to determine the PR boundary. This involves excluding the volume that undergoes reversed plastic straining from the structure and applying (10) to the reduced structure – this requires augmenting the elastic stress to the left of the inequality with a suitably chosen residual stress field. For problems involving a strong degree of cyclic thermal loading this method generally provides a conservative estimate of the PR boundary, as it essentially assumes that the volume that suffers cyclically hardens to an elastic state (A. Ponter and Karadeniz, 1985a). Perfectly plastic behaviour is considered here, and the idealisation is simple enough to determine the PR boundary through considerations of equilibrium for the assumed mechanism over the cycle.

3. Interaction diagrams

For the type of problem considered here it proves convenient to represent the different regimes of behaviour and the boundaries separating them using a Bree type interaction diagram using axes of σ_T and p.

3.1. Shakedown-reverse plasticity (SP) boundaries

First consider the response in the absence of creep. The general loading cycle is shown in Fig. 2. In the following analysis we only need consider the stress state at the four apexes of the cycle shown in Fig. 2b. Thus the times of interest are τ_i, τ_j where i, $j$take values in the range 1–4.

Note that at instant 2, $a(\tau_2) = b(\tau_2) = 1$ in Eq (8) and at instance 4, $a(\tau_4) = b(\tau_4) = 0$. These quantities take intermediate values at instants 1 and 3, which are a function of the out-of-phase factor, d. Determination of the boundary between shakedown and reverse plasticity is straightforward and simply requires determining when the elastic stress range touches the yield surface at two extremes of the cycle. Depending on the precise loading history (i.e. value of d) and how the yield strength depends on temperature this can either first occur in the hot or cold bar. We find that the elastic shakedown-reverse plasticity (SP) boundary is given by:

$$\Delta\widehat{\sigma}_c = p^s + \bar{t}_h\sigma_T^s = \sigma_{y_0} + \sigma_{y_c}(\tau_2) \quad cool\ bar \tag{SP1}$$

$$\Delta\widehat{\sigma}_h = \left|p^s - \bar{t}_c\sigma_T^s\right| = \sigma_{y_0} + \sigma_{y_h}(\tau_2) \quad for \quad d \le \bar{t}_c\sigma_T^s / p^s \quad hot\ bar \tag{SP2}$$

OR

$$\bar{t}_c\sigma_T^s\frac{d-2}{d} + p^s = \sigma_{y_0} + \sigma_{y_h}(\tau_3) \quad for \quad d > \bar{t}_c\sigma_T^s \Big/ p^s \quad hot\ bar \tag{SP3}$$

where generally $\sigma_{y_c}(\tau_2) = \sigma_{y_0}$ when $T_c \le 700\ ^\circ$C (cool bar in cold yield strength regime throughout the loading cycle – see Fig. 3a) and $\sigma_{y_c}(\tau_2) = c_1T_c + c_2$ when $T_c \ge 725\ ^\circ$C (cool bar in hot yield strength regime); note that $T_c = T_h - \Delta T$ and $\sigma_{y_h}(\tau_2) = c_1T_h + c_2$ always. For a constant yield stress, $\sigma_{y_0} + \sigma_{y_c}(\tau_2)$ and $\sigma_{y_0} + \sigma_{y_h}(\tau_2)$ are replaced by $2\sigma_{y_0} = 2\sigma_y$. The boundary SP1 applies universally since the thermal and mechanical elastic stresses in the cool bar are both tensile. This is not the case for SP2 since the thermal stress in the hot bar is compressive. For thermal delay factors below $= \bar{t}_c\sigma_T^s/p^s$, the peak compressive elastic stress magnitude in the hot bar during the cycle occurs at instance 2 (see Fig. 2), and therefore SP2 applies. At higher d the peak compressive elastic stress in the hot bar occurs at instance 3, i.e. when $= 0$, and its magnitude depends on d; SP3 gives the SP boundary for the latter. For a constant yield strength and bars of equal thickness SP1 above provides the most critical condition for a reversed plasticity mechanism. This is plotted in Fig. 4. We delay considering other situations until after we evaluate other possible mechanisms of plastic cyclic deformation, i.e. ratchetting.

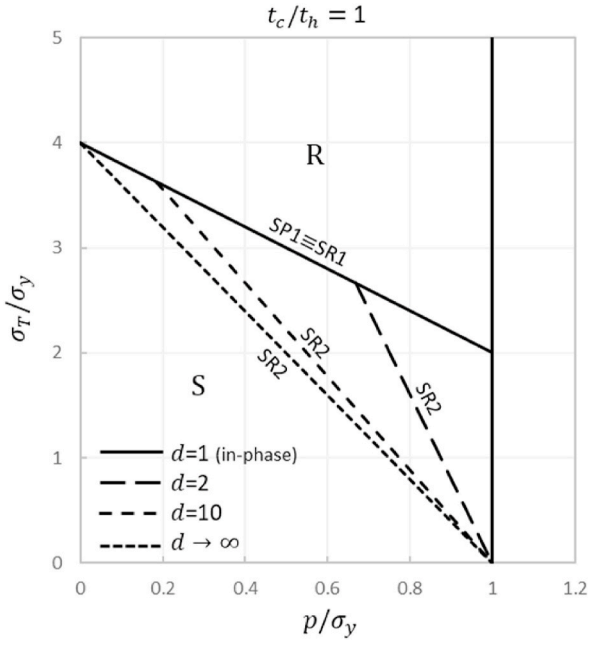

Fig. 4. Interaction diagram for constant yield stress, σ_y, and thickness ratio, $t_c/t_h = 1$, showing the effect of thermal delay factor, d.

3.2. Shakedown-ratchet (SR) boundaries

Our simplest ratchet mechanism concerns the case of in-phase loading, i.e. $d = 1$, and involves tensile plastic strains at instances 2 and 4 (see Fig. 2b) in the cool and hot bars, respectively, such that application of (10) for $d = 1$ gives:

$$\left(p^s + \bar{t}_h\sigma_T^s\right)\bar{t}_c = \sigma_{y_h}(\tau_4)\bar{t}_h + \sigma_{y_c}(\tau_2)\bar{t}_c \tag{SR1}$$

which is equivalent to the SP1 boundary when $t_c/t_h = 1$, as shown by the interaction diagram in Fig. 4 for the case of fixed yield stress, i.e. $\sigma_{y_h}(\tau_4) = \sigma_{y_c}(\tau_2) = \sigma_y$. Generally, $\sigma_{y_h}(\tau_4) = \sigma_{y_0}$, since instance 4 corresponds to room temperature; for the application here also $\sigma_{y_c}(\tau_2) = \sigma_{y_0}$, i.e. the mechanism occurs at large enough ΔT values such that the cool wall remains in the cold yield strength regime at high temperature. To determine which of SR1 and SP1 dominates beyond shakedown, we need to either evaluate the response beyond this boundary or examine how the behaviour changes as a result of small perturbations in thickness or yield strength. We demonstrate later that ratchetting (R) dominates beyond this boundary and a P regime is non-existent when $t_c/t_h = 1$. Note that here the SP2 boundary intercepts SP1 at $p/\sigma_y = 0$ (Fig. 4) but it has a positive slope and therefore it corresponds to values within the R regime (not shown); as a result the SP2 boundary is not active.

For $d > 1$ an additional mechanism exists where plasticity occurs only on loading and specifically at instance 1 in the hot bar and 2 in the cool bar (see Fig. 2). Here Eq (10) gives:

$$\left(p^s - \frac{\bar{t}_c\sigma_T^s}{d}\right)\bar{t}_h + \left(p^s + \bar{t}_h\sigma_T^s\right)\bar{t}_c = \sigma_{y_h}(\tau_1)\bar{t}_h + \sigma_{y_c}(\tau_2)\bar{t}_c \tag{SR2}$$

where the hot bar yield stress at instance 1 reads $\sigma_{y_h}(\tau_1) = c_1T_h/d + c_2$ and for the current problem $\sigma_{y_c}(\tau_2) = \sigma_{y_0}$ (large enough ΔT values). For a fixed yield stress, i.e. $\sigma_{y_h}(\tau_1) = \sigma_{y_c}(\tau_2) = \sigma_y$, and $t_c/t_h = 1$, Fig. 4 shows how the SR2 mechanism reduces the size of the shakedown regime as d is increased. For the extreme case of $d\to1$, SR2 aligns with the vertical, limit load line whereas for $d\to\infty$, SR2 dominates entirely over SR1; for intermediate d values the SR boundary is the inner envelope of SR1 and SR2.

There exists a third possible mechanism where compressive plastic strain occurs on full loading (instance 2) in the hot bar and on full unloading (instance 4) in the cool bar, such that (10) for $d = 1$ gives:

$$\left|p^s - \bar{t}_c\sigma_T^s\right|t_h = \sigma_{y_h}(\tau_2)t_h + \sigma_{y_c}(\tau_4)t_c \tag{SR3}$$

where $\sigma_{y_h}(\tau_2) = c_1T_h + c_2$ and $\sigma_{y_c}(\tau_4) = \sigma_{y_0}$. For a constant yield stress, this SR3 boundary lies well beyond SP2 and therefore it does not appear in the interaction diagrams of Figs. 4 and 5.

3.3. Reverse plasticity-ratchet (PR) boundaries

By increasing the cool bar thickness, i.e. $t_c/t_h = \bar{t}_c/\bar{t}_h > 1$, the magnitude of the thermoelastic stress, $\bar{t}_c\sigma_T$, in the hot bar increases, whereas the thermoelastic stress, $\bar{t}_h\sigma_T$, in the cool bar decreases. Consequently, in the interaction diagram the SP1 boundary translates upwards, while SP2 translates downwards, such that they cross over at given point. The inner envelope of SP1 and SP2 is shown in Fig. 5a for the cases of $t_c/t_h = 2$, $t_c/t_h = 10$ and $d = 1$; clearly, the higher the value t_c/t_h, the higher the value of p/σ_y where SP1 and SP2 cross over. The R regime beyond SP1 was identified earlier (Section 3.2) on the basis that SP1 coincides with the SR1 ratchet mechanism.

For the regime beyond SP2 we now need to identify the boundary between ratchetting and reversed plasticity (PR boundary). An example of the lower bound for the PR boundary, where the hot bar cyclically hardens to an elastic state, is given for $t_c/t_h = 2$ by the dashed line in Fig. 5a; this is determined by Ponter's method (A. Ponter and Karadeniz, 1985a) as follows. We conveniently assume that a residual stress, $\rho_h = -\widehat{\sigma}_h/2 = -(p - \bar{t}_c\sigma_T)/2$, exists such that the cyclic variation of stress in

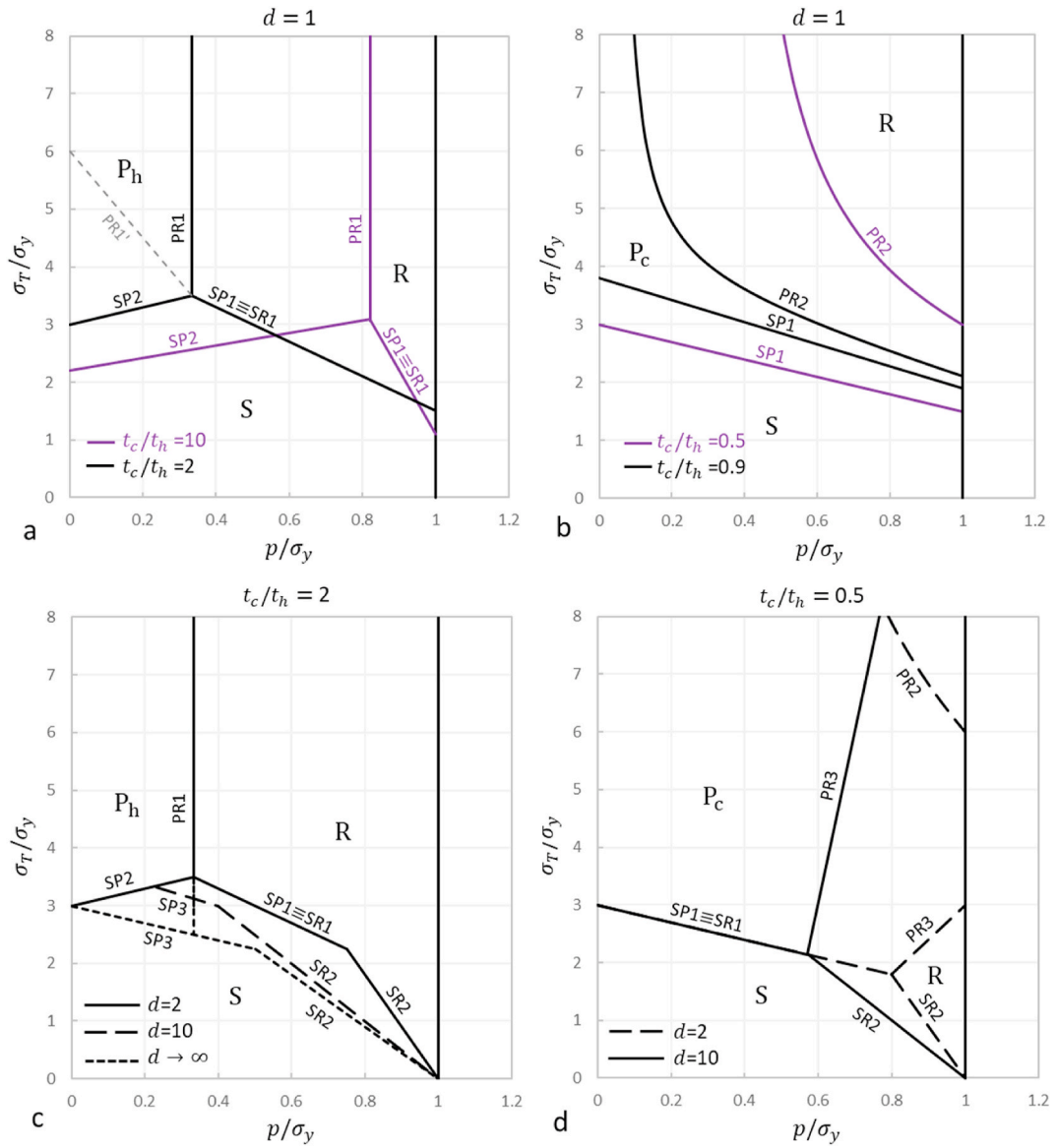

Fig. 5. Diagrams for constant yield stress, σ_y. (a) Effect of thickness ratio, t_c/t_h, in the regime $t_c/t_h > 1$ for $d = 1$. (b) Effect of t_c/t_h, in the regime $t_c/t_h < 1$ for $d = 1$. (c) Effect of delay factor, d, for $t_c/t_h = 2$. (d) Effect of delay factor, d, for $t_c/t_h = 0.5$.

the hot bar is symmetric, i.e. varies between ρ_h (no load) and $\sigma_h = \rho_h + \widehat{\sigma}_h$ (full load). By equilibrium, the stress in the cool bar will cycle between $\rho_c = -\rho_h \bar{t}_h/\bar{t}_c$ (no load) and $\sigma_c = \rho_c + \widehat{\sigma}_c$ (full load). Application of (10) only for the cool bar (the hot bar undergoes reverse plasticity) and for plasticity on full load, i.e. $d = 1$, gives the conservative PR1′ boundary:

$$\frac{(p^s - \bar{t}_c \sigma_T^s)\bar{t}_h}{2\bar{t}_c} + p^s + \bar{t}_h \sigma_T^s = \sigma_{y_c}(\tau_2) \qquad \text{(PR1')}$$

where here $\sigma_{y_c}(\tau_2) = \sigma_{y_0}$. The upper bound for the PR boundary corresponding to the perfectly plastic law of interest here is determined by postulating that tensile plastic strain occurs in the cool bar on full loading, while the hot bar undergoes reverse plasticity (P) i.e. the hot bar stress is $-\sigma_{y_h}(\tau_2)$ on full loading. Equilibrium for these conditions gives:

$$-\sigma_{y_h}(\tau_2)\bar{t}_h + \sigma_{y_c}(\tau_2)\bar{t}_c = p^s \qquad \text{(PR1)}$$

producing a vertical PR boundary which can translate from $p^s = 0$ (at $t_c/t_h = 1$) to $p^s = \sigma_y$ (at $t_c/t_h \to \infty$). This implies that P dominates over R for increasing t_c/t_h with the R region completely disappearing for $t_c/t_h \to \infty$ (note: when the yield stress is constant, i.e. $\sigma_{y_h}(\tau_2) = \sigma_{y_c}(\tau_2) = \sigma_y$, as demonstrated by Fig. 5a, whereas for the temperature dependent yield stress here $\sigma_{y_h}(\tau_2) = c_1 T_h + c_2$ and $\sigma_{y_c}(\tau_2) = \sigma_{y_0}$).

The same if found to occur, i.e. R gradually replaced by P, when t_c/t_h decreases to zero, with one difference that here the P regime is associated with cyclic plastic straining in the cool bar. Another difference here for $t_c/t_h < 1$ is that the SP1 boundary falls below the boundary for the SR1 mechanism, such that the latter no longer applies, and a P regime exists over the entire p range, as shown by Fig. 5b for the cases of $t_c/t_h = 0.9$, $t_c/t_h = 0.5$ and $d = 1$. The ratchet mechanism here is more complex than for $t_c/t_h > 1$, as it involves tensile plastic strain in the hot bar during the removal of loads, i.e. at an intermediate instance, τ_i, between 2′ and 3 (see Fig. 2b), and before the cool bar reaches yield in compression (also at an intermediate instance between 2′ and 3). Since here the instances of plastic strain are unknown, application of Ponter's extended shakedown method cannot be applied directly, as for example performed earlier for the PR1′ boundary. Due to the existence of various mechanisms of this type in the 2-bar system, conservative PR bounds based on Ponter's method will not be constructed in the rest of this paper and instead emphasis will be given on identifying the various mechanisms

and determining them based on equilibrium and the elastic solution. The resulting PR boundary is determined by considering that at the ratchet boundary the 2 bars reach yield at the same instance, τ_i, during unloading, one in tension and the other in compression, which is determined by the following system:

$$\sigma_{y_c}(\tau_{2'})\bar{t}_c + \sigma_h(\tau_{2'})\bar{t}_h = p^s \quad \text{(PR2a)}$$

$$\sigma_h(\tau_{2'}) - \lambda\left(p^s - \bar{t}_c\frac{\sigma_T^s}{d}\right) = \sigma_{y_h}(\tau_i) \quad \text{(PR2b)}$$

$$\sigma_{y_c}(\tau_{2'}) - \lambda\left(p^s + \bar{t}_h\frac{\sigma_T^s}{d}\right) = -\sigma_{y_c}(\tau_i) \quad \text{(PR2c)}$$

where $\sigma_h(\tau_{2'})$ is the actual hot bar stress on full load, i.e. at instance 2′, λ is the (unknown) unloading factor that multiplies the elastic solution in each bar and depends on the instance, τ_i, at which our assumed condition is met and $\sigma_{y_h}(\tau_i)$, $\sigma_{y_c}(\tau_i)$ are the hot bar and cool bar yield stresses corresponding to the instance, τ_i. In practical design situations the peak surface temperature is fixed and the cooling air flow can be controlled to give a particular ΔT between the two walls. The present mechanism is generally found to occur at high σ_T values, and therefore high ΔT, when the system is cooled. In practice $\sigma_{y_h}(\tau_i) = \sigma_{y_c}(\tau_i) = \sigma_{y_0}$, i.e. the bars are always in the cold yield strength regime (Fig. 3a) when plasticity occurs simultaneously in the 2 bars. The system PR2(a-c) can be used to determine λ, σ_T^s and p^s, and therefore determine the intermediate instance at which plastic deformation occurs in the 2 bars, as well as the values of $\sigma_T^s - p^s$ on the PR boundary corresponding to the PR2 mechanism. This is plotted in Fig. 5b for fixed yield stress, σ_y. It is shown that PR2 is strongly non-linear and that its shape is sensitive to $t_c/\,t_h$. For $t_c/\,t_h = 0.99$ the PR2 boundary virtually coincides with the $p = 0$ asymptote and the SP1 boundary/asymptote (Fig. 5b), practically reducing to the case of $t_c/t_h = 1$ shown earlier in Fig. 4. At the extreme $t_c/\,t_h \to 0$ the PR2 boundary translates upwards to extreme$p$ and σ_T levels, again indicating that ratchetting vanishes at extreme t_c/t_h ratios.

In contrast to the PR1 boundary which is independent of the delay factor, d, the PR2 boundary is sensitive to d. This is demonstrated in Fig. 5c and d for $t_c/t_h = 2$ and $t_c/t_h = 0.5$, respectively. In Fig. 5d the PR2 boundary occurs at much higher σ_T for $d = 2$ compared to the case $d = 1$ in Fig. 5b for the same $t_c/t_h = 0.5$ ratio; at $d = 10$ the boundary goes to large σ_T and is not shown. In terms of the SR2 boundary, in both Fig. 5c–d the effect of d is similar to the one shown earlier in Fig. 4, in that with increasing d the SR2 mechanism dominates over SR1 (or SP1), and the R region extends. The mechanism that separates the R and P regions in Fig. 5b (and generally for $t_c/t_h < 1$ and $d > 1$) involves plasticity in the hot bar at instance 1 (see Fig. 2b for $d > 1$) and is given by:

$$\rho_h\bar{t}_h + \sigma_{y_0}\bar{t}_c = 0 \quad \text{(PR3a)}$$

$$\rho_h + p^s - \bar{t}_c\frac{\sigma_T}{d} = \sigma_{y_h}(\tau_1) \quad \text{(PR3b)}$$

where ρ_h is the residual stress in the hot bar at zero load, i.e. instance 4, and $\sigma_{y_h}(\tau_1)$ is the hot bar yield stress at instance 1; in practice $\sigma_{y_h}(\tau_1) = \sigma_{y_0}$ as it is found that at instance 1 the hot bar is still in the cold yield strength regime of Fig. 3a. The PR3 boundary along with SR2 define a triangular R region in Fig. 5d, whose size increases with increasing d.

3.4. Effect of the temperature dependence of the yield stress

So far, the various interaction diagrams we have presented are for a constant yield stress. A key feature that changes when the yield stress varies with temperature according to Fig. 3a, is the structural limit load, p_L, which is given by $p_L = \sigma_{y_h}\bar{t}_h + \sigma_{y_c}\bar{t}_c$ and takes a trilinear form in a $\sigma_T - p$ diagram, relevant to the trilinear yield stress model in Fig. 3a. An example is shown in Fig. 6 for fixed $T_h = 900\ ^\circ$C (Note: the temperature of the cool bar when there is a temperature difference is $T_c = T_h - \Delta T$, where ΔT is proportional to σ_T – hence, as σ_T is increased the temperature of the cool bar reduces for fixed T_h). The vertical boundary L1 implies that the cool bar is in the cold yield strength regime in Fig. 3a, i.e. $\sigma_{y_c} = \sigma_{y_0}$ due to $T_c = T_h - \Delta T \le 700\ ^\circ$C, whereas for the L2 limit (see Fig. 6) the cool bar is in the hot regime, i.e. $\sigma_{y_c} = c_1(T_h - \Delta T) + c_2$. In the transpiration cooling application here, the hot bar is always in the hot regime in the hot part of the cycle such that $\sigma_{y_h} = c_1 T_h + c_2$. Interaction diagrams are constructed here for fixed values of T_h and are normalised by the average yield stress, $\overline{\sigma}_y = (\sigma_{y_h} + \sigma_{y_0})/2$, corresponding to the cyclic temperature range, such that $\overline{\sigma}_y$ decreases with increasing T_h.

Comparison of Fig. 6a for $T_h = 900\ ^\circ$C against Fig. 7a for $T_h = 1100\ ^\circ$C indicates that the L2 limit extends with increasing T_h, reducing the load carrying capacity, p_L, of the structure at low ΔT values; L1 is not affected. On the other hand, comparison between Fig. 7a–d indicates that L1 translates to higher p_L values with increasing t_c/t_h, and the L2 boundary extends but becomes less vertical, such that the load carrying capacity of the structure increases in the entire ΔT range.

The red-orange-brown boundaries and associated C, CR, CP regimes in Figs. 6–7, 9 involve creep phenomena which will be evaluated in Section 3.5; these boundaries are not shown in Figs. 6b and 8 for illustration purposes. The discussion here is in the absence of creep. The grey boundaries in Figs. 6–7 enclose the purely elastic regime determined by equating the elastic solution for each bar with the corresponding yield stress; ES1 and ES2 correspond to the hot and cool bar, respectively. One difference of Fig. 6a with Fig. 4 shown earlier for fixed yield stress, is that a P regime exists for the hot bar despite $t_c/t_h = 1$. This is because the SP2 boundary has shifted downwards due to the temperature dependence of the yield stress, with the effect being more pronounced as T_h is increased to 1100 °C in Fig. 6a. The transition between the SP1≡SR1 and SR2 boundaries for out-of-phase loading, i.e. $d > 1$ (Fig. 6b) occurs in the same manner as in Fig. 4.

The PR boundary for $t_c/t_h \ge 1$ in Figs. 6, 7a-b is different than the one shown earlier in Fig. 5a,c for constant yield stress. The mechanism here involves tensile plastic strain of the cool bar during loading, i.e. at an unknown instance, τ_i, before the hot bar reaches yield in compression (also during loading) and is determined by the same approach used to determine PR2 earlier. By considering that the hot bar stress at the extremes of the cycle is bounded by yield, i.e. the P regime, and by assuming that the 2 bars reach yield at the same instance, τ_i, during loading, gives the system:

$$\rho_c\bar{t}_c + \sigma_{y_0}\bar{t}_h = 0 \quad \text{(PR4/PR4a')}$$

$$\sigma_{y_0} + \kappa p^s - \lambda\bar{t}_c\sigma_T^s = -\sigma_{y_h}(\tau_i) \quad \text{(PR4/PR4b')}$$

$$\rho_c + \kappa p^s + \lambda\bar{t}_h\sigma_T^s = \sigma_{y_c}(\tau_i) \quad \text{(PR4/PR4c)}$$

where ρ_c is the residual stress in the cool bar at zero load and $\sigma_{y_h}(\tau_i)$, $\sigma_{y_c}(\tau_i)$ are the hot bar and cool bar yield stresses corresponding to the assumed instance of yielding during loading; similar to PR2, this mechanism occurs at large ΔT, such that $\sigma_{y_h}(\tau_i) = \sigma_{y_c}(\tau_i) = \sigma_{y_0}$; λ is the (unknown) loading factor for the thermoelastic stress solution and κ takes two possible values:

PR4 - $\kappa = \lambda$ for in-phase loading, i.e. $d = 1$, which produces the linear PR4 boundary in Figs. 6a, 7a-b; or PR4'- $\kappa = 1$ for significant delay factors of $\sim d > 1.5$ whereby the instance of plasticity occurs after the maximum p has been applied, i.e. between instances 3 and 4 in Fig. 2b, producing the slightly non-linear PR4′ boundary in Figs. 6b and 8a.

By increasing t_c/t_h the PR4 limit translates and rotates, such that P in the hot bar dominates over R, as shown in Fig. 7b for $t_c/t_h = 2$. However, the nature of the interaction diagram and the dominant mechanisms do not change, i.e. compare Fig. 7a–b. On the other hand, a slight change of t_c/t_h below $t_c/t_h = 1$ changes entirely the response, as shown in Fig. 7c

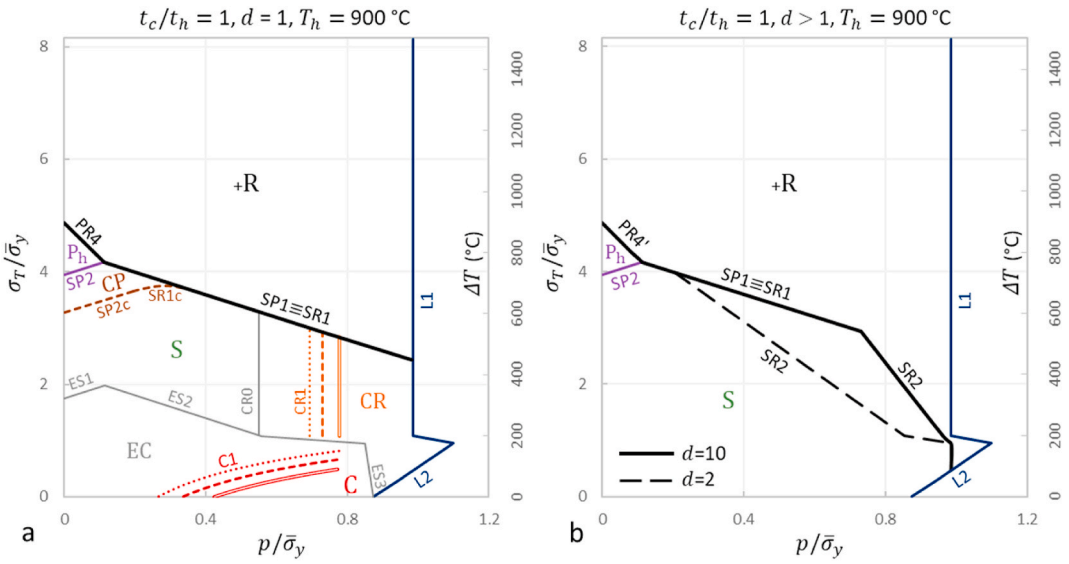

Fig. 6. Diagrams for the temperature dependent yield stress model of Fig. 3a and a hot bar temperature, $T_h = 900$ °C, and $t_c/t_h = 1$. (a) In-phase loading ($d = 1$). (b) Effect of out-of-phase phase loading ($d > 1$). The red-orange-brown boundaries are induced by creep. (For interpretation of the references to colour in this figure legend, the reader is referred to the Web version of this article.)

for $t_c/t_h = 0.9$. Firstly, this is because for $t_c/t_h < 1$ the SR3 mechanism now lies below the SP2 boundary, replacing P with an R regime. Secondly, the SP1 boundary now does not coincide with SR1 but instead falls below the latter, giving rise to a P regime for cyclic plastic deformation in the cool bar (see Fig. 7c). Beyond this P regime, i.e. at higher σ_T, the PR2 mechanism occurs in the same manner as shown earlier in Fig. 5b for fixed constant stress, with the difference being that here (Fig. 7c), at large σ_T, the boundary becomes an 'RR' boundary, separating a regime where ratchetting occurs in the compressive direction (-R) and a regime where it occurs in the tensile direction (+R). The PR1 boundary is also present in Fig. 7c (and Fig. 7d) as in Fig. 5a,c, with the only difference that in Fig. 7c–d the P regime represents cyclic plastic straining in the cool bar. By decreasing t_c/t_h further, all the above phenomena continue to occur, i.e. compare Fig. 7c–d, with the difference that for a low ratio, e.g. $t_c/t_h = 0.6$ (Fig. 7d), the –R regime shrinks and +R is pushed to large values of σ_T.

The effect of out-of-phase loading, i.e. $d > 1$, illustrated in Fig. 8a–c, is similar to that shown earlier in Fig. 5d for fixed yield stress, in that out-of-phase loading induces the SR2 and PR3 mechanisms which enclose a triangular R region that gets larger as d increases. For the cases of Fig. 8b–c, the factor d causes the PR2 boundary to translate to large σ_T values, beyond the range of interest (not shown).

3.5. The inclusion of creep deformation on the interaction diagrams

So far, time independent plastic behaviour has been assumed, where the cyclic time, t_{cycle}, and transient times,$t_{p-trans}$, $t_{\Delta T-trans}$, does not have any physical meaning. We now consider the possibility of creep strain accumulating in both bars during the steady state period of thermal loading (from instance 2 to 2′ in Fig. 2a), which we refer to as a 'creep dwell' of period, t_{dwell}. This cyclic response now depends on t_{dwell}, which is explored for fixed $t_{p-trans} = t_{\Delta T-trans} = 0.02$ h, $t_{cycle} = 2$ h and $d = 1$, such that $t_{dwell} = 1.96$ h. Creep causes four distinct effects here:

- increases the reverse plasticity region in the hot bar by inducing a CP regime in which creep deformation contributes to the cyclic plastic straining during the hot part of the cycle (Figs. 6a, 7a-b),
- increases the compressive ratchetting regime (-R) by inducing an -Rc regime in which creep deformation contributes to the ratchet mechanism (Fig. 7c–d),
- gives rise to a creep ratchetting regime (CR) at high mechanical load,
- gives rise to a global creep regime (C) at low ΔT values, i.e. high temperature in both bars.

Creep in the cool bar occurs only in the C regime, as the other regimes occur at high ΔT, i.e. low T_c. The above regimes occur in the same manner regardless of the out-of-phase factor, d, and for this reason the regimes are not denoted again in Fig. 8; note, however, that when the CR regime overlaps with the SR2 mechanism in Fig. 8, the latter dominates in the overlapping region.

3.5.1. Creep enhanced cyclic plasticity – the CP regime

The CP regime as defined here can be considered as a reverse plasticity regime, but it differs from P in that the tensile plastic strain in the hot bar on unloading is balanced by a creep compressive strain accumulated during t_{dwell}, instead of a compressive plastic strain. The boundary SP2c that separates CP from shakedown S (Figs. 6a, 7a-b) is found by reducing the yield stress range in SP2 by the amount of stress relaxation, $\Delta\sigma_{hcr}$, that occurs in the hot bar during t_{dwell} when the stress at the beginning of the dwell is σ_{y_h}:

$$\widehat{\sigma}_h = \left|p^s - \bar{t}_c\sigma_T^s\right| = \sigma_{y0} + \sigma_{y_h}(\tau_2) - \Delta\sigma_{hcr} \quad \textit{hot bar} \tag{SP2c}$$

where $\Delta\sigma_{hcr}$ is computed as follows. By using Eqs (5) and (6) for the hot bar in the kinematic condition for equal total strain rates between the bars as well as using equilibrium we get:

$$\frac{\dot{\sigma}_h}{E} + \dot{\varepsilon}_o\left(\frac{|\sigma_h|}{\sigma_o}\right)^n \exp(x) = \frac{\dot{\sigma}_c}{E} \tag{11a}$$

$$\dot{\sigma}_h\bar{t}_h + \dot{\sigma}_c\bar{t}_c = 0 \tag{11b}$$

where $x = -\frac{Q}{R}\left(\frac{1}{T_h} - \frac{1}{T_o}\right)$. By integrating Eq (11a) over t_{dwell}, i.e. between instances 1 and 1′ for $d = 1$, we obtain the stress at the end of the dwell, $\sigma_h(\tau_{1'})$, based on the stress at the beginning of the dwell, σ_{y_h}, and therefore the stress at the end of the dwell $\Delta\sigma_{hcr}$, given by:

$$\sigma_h(\tau_{1'}) = \sigma_{y_h}(\tau_2)\frac{1 + \frac{t_c}{t_h}}{\left[1 + \frac{t_c}{t_h} + (n-1)E\frac{\dot{\varepsilon}_o}{\sigma_o^n}t_{dwell}\left|\sigma_{y_h}\right|^{n-1}\exp(x)\right]^{\frac{1}{n-1}}} \tag{12a}$$

$$\Delta\sigma_{hcr} = \sigma_{y_h}(\tau_2) - \sigma_h(\tau_{1'}) \tag{12b}$$

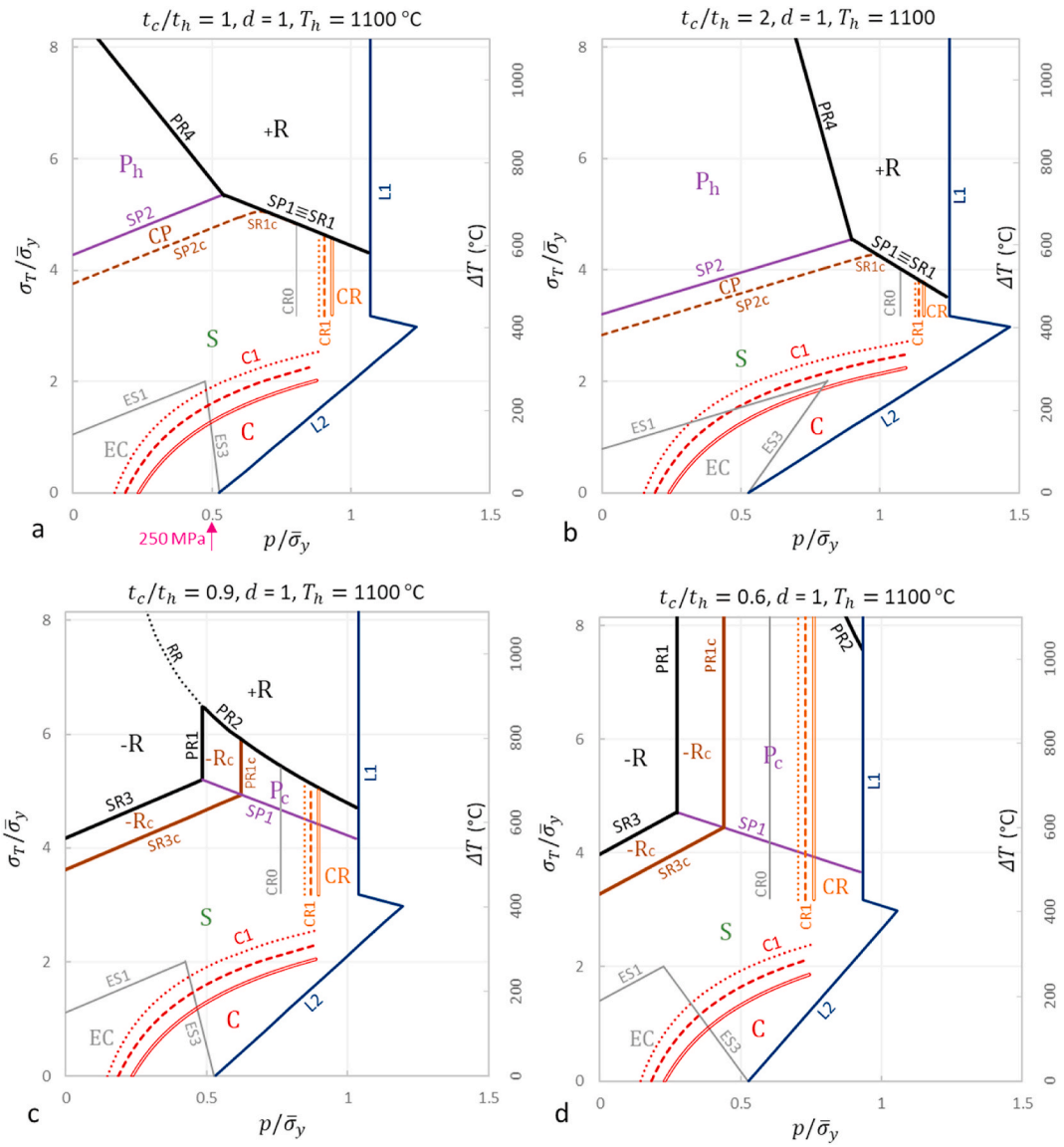

Fig. 7. Interaction diagrams for the temperature dependent yield stress model of Fig. 3a and an extreme hot bar temperature, $T_h = 1100$ °C, and $d = 1$, showing the effect of thickness ratio, t_c/t_h. (a) $t_c/t_h = 1$, (b) $t_c/t_h = 2$, (c) $t_c/t_h = 0.9$, (d) $t_c/t_h = 0.6$. The red-orange-brown boundaries relate to the creep behaviour and are for a dwell time, t_{dwell} of 1.96 h. (For interpretation of the references to colour in this figure legend, the reader is referred to the Web version of this article.)

A similar modification can be applied to the expression for the SR1 mechanism, by reducing the cool bar yield stress, σ_{y_c}, by the amount of stress relaxation in the cool bar that occurs as a consequence of relaxation in the hot bar. This gives a SR1c boundary which may only be visualised clearly in Fig. 6a, in the form of a very small curve connecting the SP2c and SR1 boundaries. The observation that the SR1c boundary merges with both SP2c and SR1 boundaries adds theoretical value to the analysis, but the fact that SR1c reaches the SR1 asymptote very quickly indicates a minor effect of creep on SR1 and a low practical significance; for this reason we will not give the calculation details for SR1c.

3.5.2. Creep enhanced ratchetting – the R_c regime

The modification of the SR3 limit into SR3c and PR1 into PR1c in Fig. 7c–d due to creep, where here the subscript "c" now indicates a boundary with R_c, is a well pronounced effect. The difference in the extent of the -Rc regime compared to –R is that compressive creep strain occurs during t_{dwell} in the hot bar (instead of plastic strain) on full loading. In this regard, SR3c and PR1c are determined again by compensating for the relaxed stress, $\Delta\sigma_{hcr}$ (given by Eq (12)) in the original SR3 and PR1 expressions, as follows:

$$\left|p^s - \bar{t}_c\sigma_T^s\right|t_h = \left(\sigma_{y_h}(\tau_2) - \Delta\sigma_{hcr}\right)t_h + \sigma_{y_c}(\tau_4)t_c \quad \text{(SR3c)}$$

$$-\left(\sigma_{y_h}(\tau_2) - \Delta\sigma_{hcr}\right)\bar{t}_h + \sigma_{y_c}(\tau_2)\bar{t}_c = p^s \quad \text{(PR1c)}$$

Note that the position of these boundaries are sensitive to the chosen dwell times and creep properties of the material. In Fig. 7 a dwell time of 1.96 h has been assumed. The effect of dwell time on these boundaries is illustrated in Fig. 9, which is discussed later.

3.5.3. Creep ratchetting (CR) regime

Creep induced ratchetting (CR) occurs when the hot bar experiences a large enough tensile stress during t_{dwell} (occurs at high p values) while the cool bar is at yield (tension), such that the stresses cannot relax in the system. As a result, tensile creep strain accumulates in the hot bar under constant stress (and thus constant rate) and simultaneously the same plastic strain accumulates in the cool bar to satisfy kinematics. CR0 in Figs. 6a and 7 is the vertical limit where the stress in the hot bar at the beginning of the creep dwell is zero; since the cool bar is at yield, CR0 is

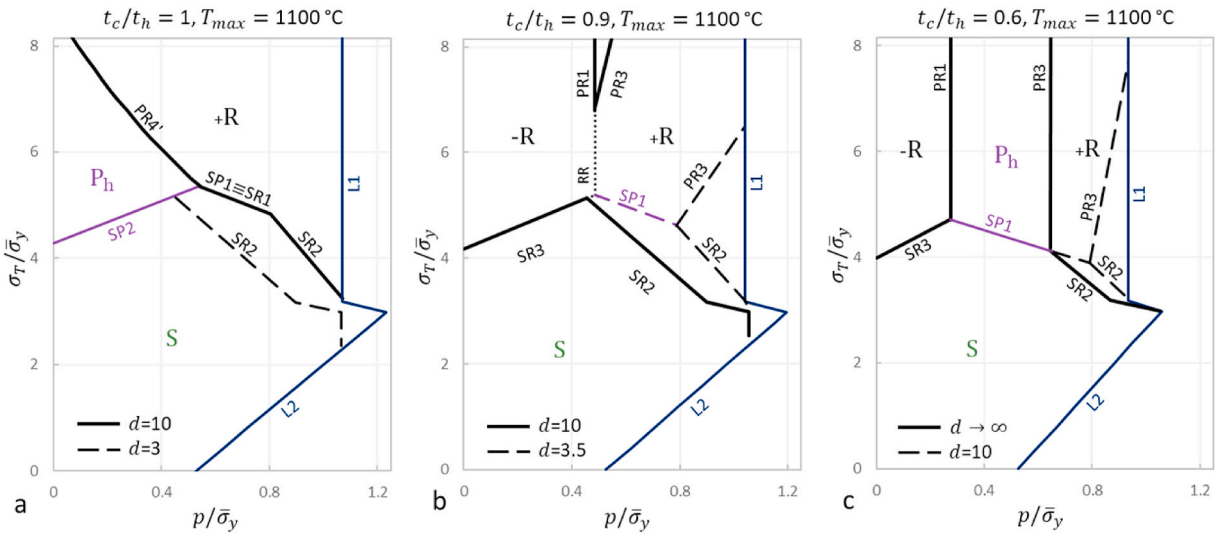

Fig. 8. Interaction diagrams for the temperature dependent yield stress model of Fig. 3a and an extreme hot bar temperature, $T_h = 1100$ °C, showing the effect of thermal delay factor, d, for three thickness ratios, t_c/t_h. (a) $t_c/t_h = 1$, (b) $t_c/t_h = 0.9$, (c) $t_c/t_h = 0.6$.

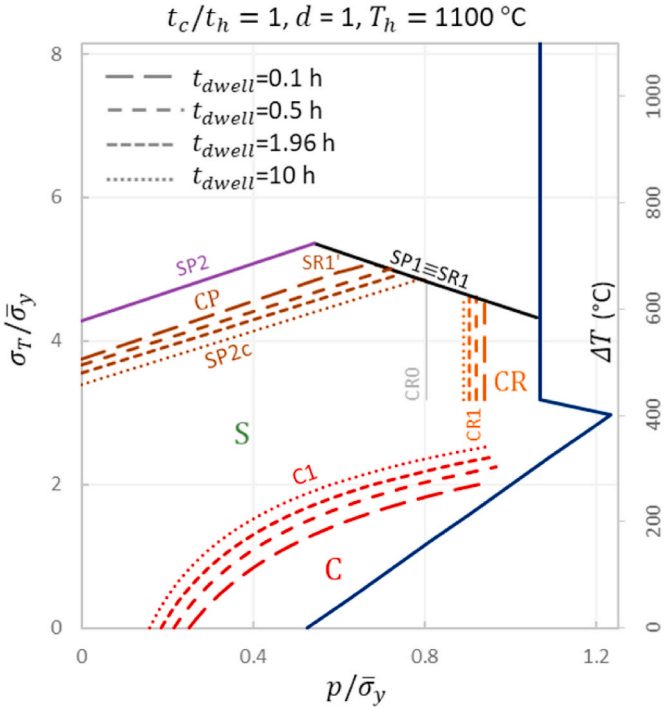

Fig. 9. Diagram for the temperature dependent yield stress model of Fig. 3a with $T_h = 1100$ °C, $d = 1$, $t_c/t_h = 1$, showing the effect of creep dwell time, t_{dwell}, on the creep induced boundaries SP2c, CR1, C1.

given by $\sigma_{y_0}\bar{t}_c = p_{CR}$ (equilibrium). For the creep law used here, however, the CR phenomenon becomes significant at considerably larger p than the CR0 limit, p_{CR}. This is demonstrated in Figs. 6a and 7 by plotting three lines representing $N_{0.1} = 10^5$, $N_{0.1} = 10^4$ and $N_{0.1} = 10^3$ (for ascending p) cycles required for a $\varepsilon_{cr_{0.1}} = 0.1$ total creep strain accumulation. For each N the value of p_{CR} is found by determining the constant creep stress, σ_h, via equilibrium and using it in the creep law, as given below:

$$\sigma_h\bar{t}_h + \sigma_{y_0}\bar{t}_c = p_{CR} \qquad \text{(CR1/C1a)}$$

$$\varepsilon_{cr_{0.1}} = N_{0.1}\, t_{dwell}\dot{\varepsilon}_o \left(\frac{|\sigma_h|}{\sigma_o}\right)^n \exp(x) \qquad \text{(CR1/C1b)}$$

3.5.4. *Global creep (C) regime*

When creep occurs in both bars, after a transient period the system reaches a cyclic state whereby the 2 bars creep in tension at the same rate (during t_{dwell}) at constant stresses, σ_h and σ_c. These stresses are determined by equilibrium and by using Eq (5) for $\dot{\varepsilon}_{cr_h} = \dot{\varepsilon}_{cr_c}$, giving the relations:

$$\sigma_h\bar{t}_h + \sigma_c\bar{t}_c = p_C \qquad \text{(C1a)}$$

$$\sigma_h^n x_h = \sigma_c^n x_c \qquad \text{(C1b)}$$

where $x_h = \exp\left(-\frac{Q}{R}\left(\frac{1}{T_h}-\frac{1}{T_o}\right)\right)$ and $x_c = \exp\left(-\frac{Q}{R}\left(\frac{1}{T_c}-\frac{1}{T_o}\right)\right)$ with $T_c = T_h - \Delta T$ and $\Delta T = \sigma_T/E\alpha$. By using again the CR1(b) expression for either σ_h or σ_c, we construct the C1 contours in Figs. 6a and 7 representing $N_{0.1} = 10^5$, $N_{0.1} = 10^4$ and $N_{0.1} = 10^3$ (for ascending p at $\sigma_T = 0$) cycles for a $\varepsilon_{cr_{0.1}} = 0.1$ total creep strain accumulation; note that these contours insensitive to the chosen value of t_c/t_h (Fig. 7a–d). These plots are for a dwell time of 1.96 h. The effect of dwell time, t_{dwell}, on the SP2c, CR1 and C1 boundaries is illustrated in Fig. 9; for CR1, C1 here we consider $N_{0.1} = 10^4$ cycles for $\varepsilon_{cr_{0.1}} = 0.1$ total creep strain accumulation.

4. Discussion

All our analytical results presented in Figs. 4–9 were verified via FE simulations (not shown); experiments that can further support these results will be considered in future studies. In the following discussion we will focus on the implications of our results for the double wall transpiration cooling (DWTC) application. The expected loading range for Ni-based DWTC turbine blades includes thermal differences, ΔT, within the range 100–300 °C and centrifugal stress, p, up to 250 MPa (Skamniotis et al., 2021). At first glance, our results here suggest that the structure is safe in terms of global failure mechanisms, even when the extreme temperature $T_h = 1100$ °C. The above ΔT range taken from previous reports (Ngetich et al., 2019; Skamniotis et al., 2021), however, concerns standard volumetric coolant flow rates, regions of high film cooling effectiveness and also encapsulates a thermal gradient, ΔT_h, through the hot wall thickness and thus concerns the global thermal difference between the external surface of the hot wall and the internal surface of the cool wall; such effects have not been studied here. The fast

development of DWTCs and film cooling can give rise to different ΔT values with different contributions of ΔT_h (Skamniotis et al., 2021). Simultaneously, the centrifugal stress, p, reduces from a maximum value, at the blade root section, down to zero at the blade tip, indicating that a range of load combinations occur along the length of a turbine blade. Firstly, this suggests that when ratchetting occurs under a given load combination, this may be in a local region of the blade. Secondly, it suggests that design should consider a wide range of thermomechanical loading scenarios, not only due to the variation of p but also the difficulty in predicting the details of thermal loading in different blade regions for different geometries and under different cooling conditions. This adds value to our results here, in that they provide the full landscape for the possible global failure mechanisms.

Reverse plasticity-ratchetting (PR) boundaries presented here lie beyond the current expected loading range as they occur at very high ΔT levels. The same mainly applies for classical shakedown-ratchetting (SR) boundaries as well as for creep induced ratchetting (CR) phenomena, which occur at both high ΔT and p values. An exception is the case of low thickness ratio, $t_c/t_h < 1$ (Fig. 7c–d) where compressive ratchetting (-R) can occur at zero mechanical loads and at decreasing ΔT levels as $t_c/\ t_h$ decreases. This is a key result because a low t_c/t_h has been associated (Skamniotis et al., 2021; Skamniotis and Cocks, 2021b) with better fatigue performance at the film cooling holes, since it reduces the thermal stresses in the hot plate. Hence, our results here suggest a trade-off between ratchetting and fatigue, posing a limit to the degree by which the t_c/t_h ratio can be reduced.

Creep failure (C) is also an important concern, as here it occurs near the current expected loading range when the hot bar is at the extreme temperature, $T_h = 1100\ ^\circ$C (Figs. 7–8), providing a lower bound to the desirable ΔT range. The creep failure boundary of interest to turbine blades is the one corresponding to $N_{0.1} = 10^4$ cycles for a total creep strain of 0.1. With decreasing T_h, creep failure becomes unlikely, as for example shown in Fig. 6a for the lower extreme $T_h = 900\ ^\circ$C. A lower maximum temperature has also been associated with better fatigue performance at the film cooling holes, due to a lower degradation of the yield strength (Skamniotis and Cocks, 2021b). Therefore, our result here strengthens the argument that the permissible peak metal temperature is a key parameter in terms of overall mechanical performance and should be balanced against the benefits of using hotter gas temperatures.

The currently predicted structural creep rates (C1 curves in Fig. 7), however, do not take into account that in practise a thermal gradient, ΔT_h, occurs through the hot wall thickness, reducing the volume of material experiencing extreme temperatures. On the other hand, the gradient, ΔT_h, may significantly modify the current SR and PR boundaries, by introducing different mechanisms of relevance to the ones occurring in the Bree problem (Bree, 1967). We anticipate that the ratchet boundaries will become non-linear, since the volume of material experiencing plastic straining at given instances through the cycle in the hot wall will change with the level of thermal loading. These effects were not studied here, firstly because they would complicate the understanding of the various ratchetting mechanisms driven by the interaction of the 2 bars through membrane stresses alone. Secondly, membrane stresses arising from the average temperature difference in the walls typically dominate over bending stresses in the hot wall arising from the ΔT_h gradient (Skamniotis et al., 2021). All the above arguments surrounding the potential effects of ΔT_h will be explored in a later study where we will employ the same analytical methodology using more elaborate temperature fields.

The effect of a 3D biaxial stress field will also be analysed in this future study, along with the effect of cooling holes. In the absence of holes, we anticipate that the ratchet mechanisms identified here in 2D will occur in a similar manner in 3D, but the corresponding boundaries will change depending on the type of yield surface considered in the material constitutive law. The addition of holes will reduce the structural load carrying capacity and also induce stress concentrations. These will respectively result in localised ratchetting at the minimum cross section of the plates, i.e. local thinning mechanisms, and in an expansion of the reverse plasticity (P) regions (Adibi-Asl and Reinhardt, 2010; Ma et al., 2021). Therefore, we expect that P will dominate in the interaction diagrams and that strongly non-linear PR boundaries will exist, which are generally known to be highly sensitive to the material hardening law (Karadeniz and Ponter, 1984; A. Ponter and Karadeniz, 1985b). In this case, conservative PR bounds may be derived by assuming cyclic hardening (of the material in the P regime) to an elastic state, through the method developed by Ponter (A. Ponter and Karadeniz, 1985a) and compared against upper PR bounds of the type presented here based on perfect plasticity. Comparison of our present results for the simplified structure against 3D solutions including holes will be valuable for design, by revealing the degree by which porosity influences global ratchetting in thin wall structures. While analytical solutions may be possible for coupled thin plates with transverse holes, the actual case of thick plates with inclined film holes as shown in Fig. 1b may be impossible to tackle analytically. However, analytical solutions for idealised geometries can be vital for identifying key effects as well as interpreting results for the full problem obtained from both indirect and direct methods (Ma et al., 2021; K. V. Spiliopoulos and Panagiotou, 2012; Zhu et al., 2017).

5. Conclusions

Analytical solutions to the problem of coupled bars under thermomechanical loading provide a useful strategy for understanding and evaluating global ratchetting (R) and creep failure mechanisms in dual wall transpiration cooling systems (DWTC). This aids in solving the complexity of design for turbine blade and hypersonic flight applications.

The use of elastic stress solutions in Koiter's shakedown theorem in combination with equilibrium relations provides all the possible elastic shakedown-ratchet (SR) and reverse plasticity-ratchet (PR) boundaries for a constant or temperature dependent yield stress. Despite the simplicity of the 2-bar structure and the perfectly plastic law used here, non-linear PR boundaries exist due to the fact that plastic strains do not always occur at the extremes of the loading cycle. The ratchetting region is maximised when the thermoelastic stresses are of the same magnitude in the 2 bars, i.e. when they have the same thickness, and is minimised at large thermoelastic stress differences, i.e. large thickness differences, where reverse plasticity (P) in one of the bars dominates.

Out-of-phase loading associated with the delay of temperature build up in the system, is found to increase the ratchetting regime, although for Ni-based turbine blade systems this tends to be at extreme thermomechanical loading conditions beyond the current practical range. Key pointers for design are:

(a) a low cool bar thicknesses can activate a compressive ratchetting mechanism,
(b) creep in the cool bar should be avoided as it can activate creep failure when significant mechanical stresses are applied,
(c) the maximum temperature in the hot bar plays a critical role for both ratchetting and creep.

Our study provides a framework for understanding ratchetting and creep for more complex cyclic thermomechanical loading problems. It also provides a framework to evaluate numerical 3D solutions for complex transpiration cooling geometries with holes.

Author statement

Christos Skamniotis: Investigation, Writing – original draft preparation. **Alan Cocks:** Funding acquisition, Supervision, Writing-Reviewing and Editing.

Declaration of competing interest

The authors declare that they have no known competing financial interests or personal relationships that could have appeared to influence the work reported in this paper.

Acknowledgements

The work was supported by EPSRC programme grant EP/P000878/1.

References

Adibi-Asl, R., Reinhardt, W., 2010. Ratchet boundary determination using a noncyclic method. J. Pressure Vessel Technol. 132 (2).
Adibi-Asl, R., Reinhardt, W., 2011a. Non-cyclic shakedown/ratcheting boundary determination-Part 2: numerical implementation. Int. J. Pres. Ves. Pip. 88 (8–9), 321–329.
Adibi-Asl, R., Reinhardt, W., 2011b. Non-cyclic shakedown/ratcheting boundary determination-Part 1: analytical approach. Int. J. Pres. Ves. Pip. 88 (8–9), 311–320.
Bradford, R., 2012. The Bree problem with primary load cycling in-phase with the secondary load. Int. J. Pres. Ves. Pip. 99, 44–50.
Bradford, R., 2017. The Bree problem with the primary load cycling out-of-phase with the secondary load. Int. J. Pres. Ves. Pip. 154, 83–94.
Bree, J., 1967. Elastic-plastic behaviour of thin tubes subjected to internal pressure and intermittent high-heat fluxes with application to fast-nuclear-reactor fuel elements. J. Strain Anal. 2 (3), 226–238.
Dye, D., Conlon, K., Lee, P., Rogge, R., Reed, R., 2004. Welding of single crystal superalloy CMSX-4: experiments and modeling. In: Paper Presented at the Superalloys 2004 (Tenth International Symposium).
Hübel, H., 1996. Basic conditions for material and structural ratcheting. Nucl. Eng. Des. 162 (1), 55–65.
Karadeniz, S., Ponter, A., 1984. The influence of transient thermal loading on the Bree plate; A simplified method of analysis. Nucl. Eng. Des. 80 (3), 359–374.
Kauss, O., Tsybenko, H., Naumenko, K., Hütter, S., Krüger, M., 2019. Structural analysis of gas turbine blades made of Mo-Si-B under transient thermo-mechanical loads. Comput. Mater. Sci. 165, 129–136.
Koiter, W.T., 1960. General theorems for elastic plastic solids. Prog. Solid Mech. 167–221.
Ma, Z., Wang, X., Chen, H., Xuan, F.-Z., Liu, Y., 2021. A unified direct method for ratchet and fatigue analysis of structures subjected to arbitrary cyclic thermal-mechanical load histories. Int. J. Mech. Sci. 194, 106190.
Murray, A.V., Ireland, P.T., Rawlinson, A.J., 2017. An integrated conjugate computational approach for evaluating the aerothermal and thermomechanical performance of double-wall effusion cooled systems. In: Paper Presented at the ASME Turbo Expo 2017: Turbomachinery Technical Conference and Exposition.
Murray, A.V., Ireland, P.T., Romero, E., 2019. Development of a steady-state experimental facility for the analysis of double-wall effusion cooling geometries. J. Turbomach. 141 (4).
Murray, A.V., Ireland, P.T., Wong, T.H., Tang, S.W., Rawlinson, A.J., 2018. High resolution experimental and computational methods for modelling multiple row effusion cooling performance. Int. J. Turbomach., Propul. Power 3 (1), 4.
Nathal, M., Bierer, J., Evans, L., Pogue, E., Ritzert, F., Gabb, T., 2015. Stress relaxation behavior in single crystal superalloys. Mater. Sci. Eng., A 640, 295–304.
Ng, H., Moreton, D., 1987. Alternating plasticity at the surfaces of a Bree cylinder subjected to in-phase and out-of-phase loading. J. Strain Anal. Eng. Des. 22 (2), 107–113.
Ngetich, G.C., Murray, A.V., Ireland, P.T., Romero, E., 2019. A three-dimensional conjugate approach for analyzing a double-walled effusion-cooled turbine blade. J. Turbomach. 141 (1).
Ponter, A., Cocks, A., 1984. The Incremental Strain Growth of an Elastic-Plastic Body Loaded in Excess of the Shakedown Limit.
Ponter, A., Karadeniz, S., 1985a. An Extended Shakedown Theory for Structures that Suffer Cyclic Thermal Loading. Part 1: Theory.
Ponter, A., Karadeniz, S., 1985b. An Extended Shakedown Theory for Structures that Suffer Cyclic Thermal Loading. Part 2: applications.
Ponter, A.R., Karadeniz, S., Carter, K., 1990. The Computation of Shakedown Limits for Structural Components Subjected to Variable Thermal Loading-Brussels Diagrams (Retrieved from).
Reed, R.C., 2008. The Superalloys: Fundamentals and Applications. Cambridge university press.
Sadowski, T., Golewski, P., 2012. Detection and numerical analysis of the most efforted places in turbine blades under real working conditions. Comput. Mater. Sci. 64, 285–288.
Segle, P., Eklund, G., Skog, M., 2016. A two-rod testing approach for understanding ratcheting in structures. Int. J. Pres. Ves. Pip. 139, 184–193.
Sengupta, A., Putatunda, S., Bartosiewicz, L., Hangas, J., Nailos, P., Peputapeck, M., Alberts, F., 1994. Tensile behavior of a new single-crystal nickel-based superalloy (CMSX-4) at room and elevated temperatures. J. Mater. Eng. Perform. 3 (1), 73–81.
Skamniotis, C., Cocks, A.C., 2020. Minimising stresses in double wall transpiration cooled components for high temperature applications. Int. J. Mech. Sci. 189, 105983.
Skamniotis, C., Cocks, A.C., 2021c. Thermal and centrifugal stresses in curved double wall transpiration cooled components with temperature dependent thermoelastic properties. Int. J. Solid Struct. 111273.
Skamniotis, C., Courtis, M., Cocks, A.C., 2021. Multiscale analysis of thermomechanical stresses in double wall transpiration cooling systems for gas turbine blades. Int. J. Mech. Sci. 207, 106657.
Skamniotis, C.G., Cocks, A.C., 2021a. 2D and 3D thermoelastic phenomena in double wall transpiration cooling systems for gas turbine blades and hypersonic flight. Aero. Sci. Technol. 106610.
Skamniotis, C.G., Cocks, A.C., 2021b. Creep-plasticity-fatigue calculations in the design of porous double layers for new transpiration cooling systems. Int. J. Fatig. 106304.
Spiliopoulos, K., Panagiotou, K., 2014. A residual stress decomposition based method for the shakedown analysis of structures. Comput. Methods Appl. Mech. Eng. 276, 410–430.
Spiliopoulos, K.V., Panagiotou, K.D., 2012. A direct method to predict cyclic steady states of elastoplastic structures. Comput. Methods Appl. Mech. Eng. 223, 186–198.
Sunden, B., Xie, G., 2010. Gas turbine blade tip heat transfer and cooling: a literature survey. Heat Tran. Eng. 31 (7), 527–554.
Zhu, X., Chen, H., Xuan, F., Chen, X., 2017. Cyclic plasticity behaviors of steam turbine rotor subjected to cyclic thermal and mechanical loads. Eur. J. Mech. Solid. 66, 243–255.